

## Chapter 2. Testing Conditions in Kolsky Bar Experiments

In a material property characterization experiment, the specimen should deform uniformly under well-controlled testing conditions in order for the experimental results to be clearly documented and interpreted. In quasi-static experiments, testing conditions are monitored and adjusted in real time by closed-loop feedback control systems such that the specimen deforms under specified conditions throughout the test. In Kolsky-bar experiments, feedback control systems are not available. Furthermore, due to the relatively low stiffness of the bars, even under identical loading conditions, the testing conditions on the specimen depend on the specimen response. Therefore, it is challenging to subject the specimen to specified loading conditions in Kolsky-bar experiments. Both the loading processes in the specimen and their relations to the commonly defined testing conditions need to be carefully examined. In addition, the development of Kolsky bar and its data reduction scheme involves many idealized assumptions. However, in actual Kolsky-bar experiments, these assumptions are not satisfied automatically, which requires further efforts in experiment design. The valid testing conditions and necessary approaches to achieve specified conditions in the Kolsky-bar experiments are presented in this Chapter.

### 2.1 One-dimensional Planar Elastic Wave Propagation

In a Kolsky-bar experiment, the incident and transmission bars must remain linearly elastic so that the surface strains are linearly related to the stress waves inside the bars and the elastic wave theory can be employed for data reduction. A high-strength bar material such as alloy steel is therefore preferred. As indicated by (1.2), the upper limit of the striker impact speed is directly determined by the yield strength of the bar material.

The incident and transmission bars must also be sufficiently long to ensure one-dimensional wave propagation and to facilitate large deformation in the specimen when needed. [Figure 2.1](#) shows an example of stress distribution in a cross section at a distance of half of the bar diameter (37 mm) to the impact end in a conventional Kolsky-bar experiment

(Wang 2007). It clearly shows that the amplitude of axial stress decreases along the radial direction with the maximum at the center of the cross section and minimum at the bar surface. When the stress wave propagates to the distance of twice of the bar diameter, the axial stress distributes uniformly over the cross section, as shown in Fig. 2.2, but with significant oscillations. For the case shown in Fig. 2.1, the measured strain by the strain gages on the bar surface deviates from the actual bar strain. The strain gage locations thus should be far from the bar ends. In practice, they are mounted at least 10 bar diameters from both ends. Therefore, the bars should have a length-to-diameter ( $L/D$ ) ratio of at least  $\sim 20$ . Most bars, particularly the incident bar, are typically much longer than this limit. To avoid wave overlapping at the strain gage location, the incident bar is at least twice as long as the striker.

When the Kolsky bar is used to conduct dynamic experiments on hard materials with a much smaller diameter than the bar diameter, the assumption of planar wave in the bars may be violated because of elastic or plastic indentation of the specimen into the bar ends. Such an indentation introduces a significant error in the strain measurements in the specimen particularly when specimen strain is small. The indentation can also cause premature failure in the specimen due to stress concentrations at the specimen edges. In order to avoid such an indentation, high-stiffness and high-strength platens such as tool steel and tungsten carbides are placed between the bars and the specimen. The wave impedance of the platens should match with that of the bars,  $(\rho c A)_{\text{platen}} = (\rho c A)_{\text{bar}}$ , to minimize the wave disturbances caused by the introduction of the platens. This issue will be further addressed in Chapter 3.

The oscillations in Fig. 2.2 are the result of wave dispersion. Since the bar material is free to move in the radial direction, the actual stress wave in the slender bars is still two dimensional in nature; however, it may be considered to be approximately one-dimensional when dealing with axial quantities. When a compressive wave propagates along the bar axis, the material is pushed forward, which is described by the axial kinetic energy, as well as sideways, which are the radial directions due to Poisson's effects. The material acceleration in the radial directions in turn causes inertia-induced stress in the axial direction. These two-dimensional effects result in wave dispersion when propagating along the bars. The effects of dispersion accumulate as the waves propagate over distance, and become more significant when bar diameter increases.

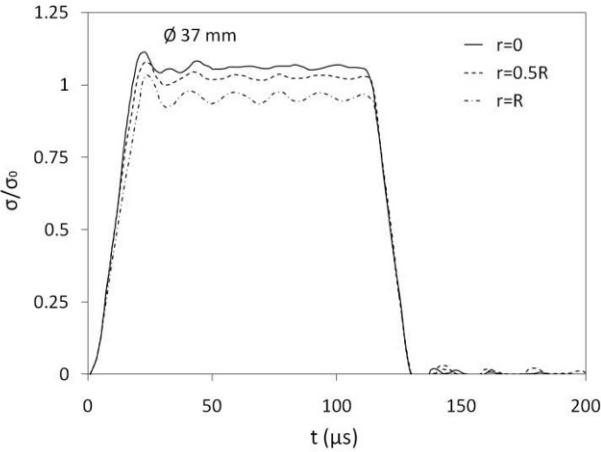


Figure 2.1 Axial stress distributions over the cross section  
0.5D from the 37-mm-diameter bar end  
(Reproduced from Wang (2007) with permission)

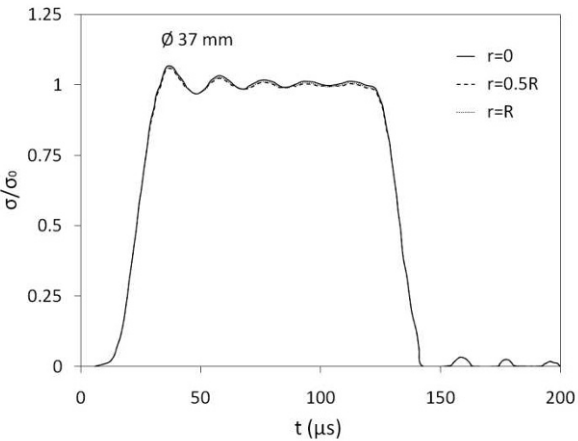


Figure 2.2 Axial stress distributions over the cross section  
2D from the 37-mm-diameter bar end  
(Reproduced from Wang (2007) with permission)

Wave dispersion has been extensively discussed starting from Pochhammer (1876) and Chree (1889). They independently solved the equation of motion for a sinusoidal wave propagating in an infinitely long cylinder. Figure 2.3 graphically shows the Pochhammer-Chree solution for wave dispersion, where  $\Lambda$  is the wave length (inversely proportional to the frequency),  $a$  is the radius of the circular cross-section of the bar in which the waves are propagating,  $C_0 = \sqrt{E/\rho}$  is the elastic bar wave speed, and  $C_p$  is the elastic wave speed of wave components with various frequencies (Kolsky 1963). The Pochhammer-Chree solution reveals that the propagation velocity of a stress wave decreases with decreasing wavelength. In other words, a high-frequency stress wave travels slower than a wave which has a lower frequency.

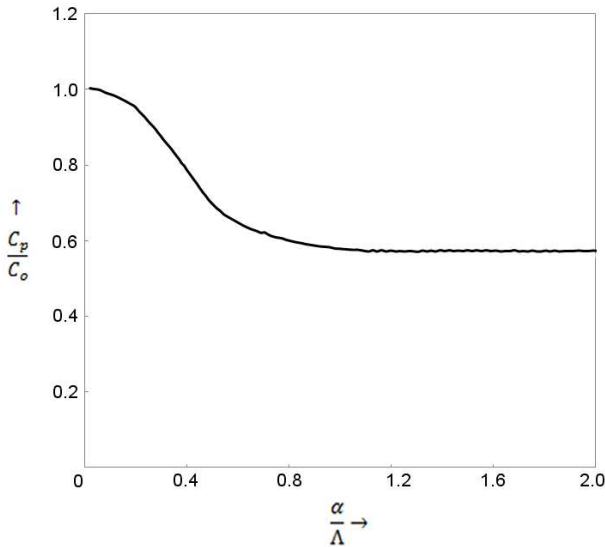


Figure 2.3 Pochhammer-Chree solution for wave dispersion ( $\nu = 0.29$ )  
(Reproduced from Kolsky (1963) with permission)

In a Kolsky-bar experiment, the ideal rectangular pulse generated by the impact of the striker on the incident bar is composed of a spectrum of frequencies. Each frequency component has its own propagating velocity. The higher frequency components of the pulse lag behind the lower frequency components after traveling a distance, resulting in a distorted waveform, which is wave dispersion as discussed above. [Figure 2.4](#) shows the wave dispersion in a Kolsky-bar experiment. The stress waves in [Fig. 2.4](#) are the incident pulse and its reflection at the free end (no transmission bar was used). Both pulses were recorded by the same strain gages in the middle location of the incident bar, so that any difference between the two pulses was caused by wave dispersion in nature rather than by errors in the data acquisition system. As seen in [Fig. 2.4](#), both incident and reflected pulses contain high frequency oscillations. A comparison of the two pulses shows that the reflected pulse differs from the incident pulse after propagating a distance of  $\sim 5700$  mm, which is the result of wave dispersion.

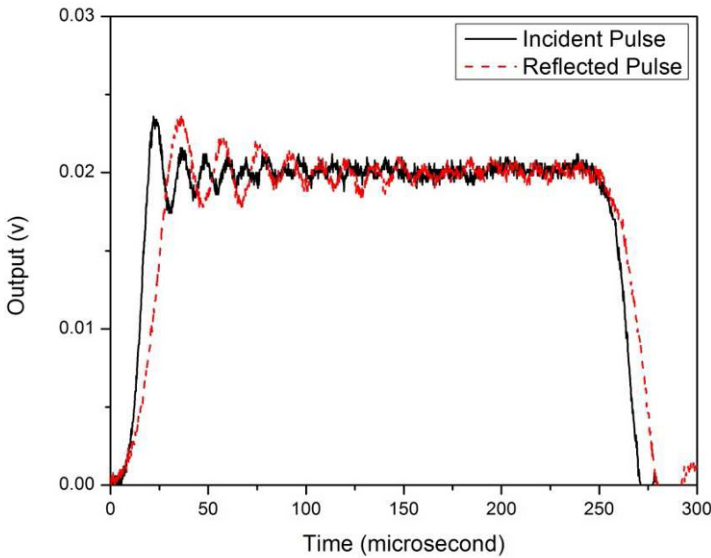


Figure 2.4. Wave dispersion in a Kolsky-bar experiment

The physics of wave dispersion has been analytically modeled. Therefore, correction for wave dispersion is possible and numerical corrections for wave dispersion have been extensively studied (Follansbee and Frantz 1983, Gorham 1983, Gong et al. 1990). Here we give an example of numerical correction through Fourier transform method originally published by Follansbee and Frantz (1983). The form of the Fourier transform of a wave  $f(t)$  at the position,  $z$ , can be expressed as

$$f(t) = \frac{A_0}{2} + \sum_{n=1}^{\infty} D_n \cos(n\omega_0 t - \delta) \quad (2.1)$$

where  $A_0$  and  $D_n$  are constants. The phase angel,  $\delta$ , is given by

$$\delta = \frac{n\omega_0 z}{C_0} \left( \frac{C_0}{C_n} - 1 \right) \quad (2.2)$$

where  $C_n$  is the propagation velocity of the frequency component  $n\omega_0$ . The dispersion can thus be corrected by adjusting the phase angle

$$\delta = \delta_0 + \frac{n\omega_0 \Delta z}{C_0} \left( \frac{C_0}{C_n} - 1 \right) \quad (2.3)$$

where  $\delta_0$  is the phase angel at  $z_0$ ; and  $\delta$  is the phase angel at  $z = z_0 + \Delta z$ . The relationship between the phase velocity and wavelength is referred to [Fig. 2.3](#).

[Figure 2.5](#) shows the waves measured by the strain gages in the middle of the incident bar (a) and predicted at the incident bar/specimen interface (b) due to wave dispersion (Follansbee and Frantz 1983). In principle, the oscillations in all three pulses (incident, reflected, and transmitted pulses) should be corrected to the specimen/bar interfaces. When the specimen is a ductile material, the transmitted pulse is not as dispersive as the incident and reflected pulse because the specimen plays a role of filter. Dispersion correction reduces the oscillations in the resultant stress-strain curve so that the measurement of stress-strain response of the specimen becomes more accurate, particularly at small strains.

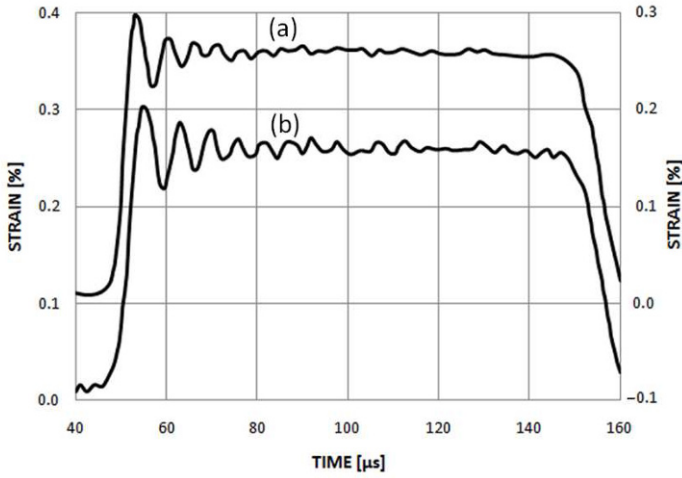


Figure 2.5 Comparison of incident wave measured by the strain gages in the middle of the incident bar (a) with that predicted at the incident bar/specimen interface (b)  
(Reproduced from Follansbee and Frantz (1983) with permission)

The wave dispersion can be physically minimized in experiments through pulse shaping techniques where a small piece of material is placed on the impact end of the incident bar as the pulse shaper. The plastic deformation of the pulse shaper physically filters out the high frequency components in the incident pulse. Figure 2.6 shows the frequency spectrum comparison of a non-shaped pulse and a shaped pulse. The components with the frequencies above 40 KHz have been filtered out in the shaped pulse such that wave dispersion is significantly minimized, as evidenced in Fig. 2.7. Figure 2.7 shows that the incident pulse is exactly the same as its reflection from the free end, which is different from those shown in Fig. 2.4. Numerical correction of the wave dispersion is not necessary when the pulse shaper is used in a Kolsky-bar experiment. The use of the pulse shaping also extends the rise time in the incident pulse, which is necessary to achieve stress equilibrium in the specimen. Furthermore, proper design of the pulse shaping facilitates constant strain rate deformation in the specimen. The detailed pulse shaping technique is presented in Chapter 2.5.

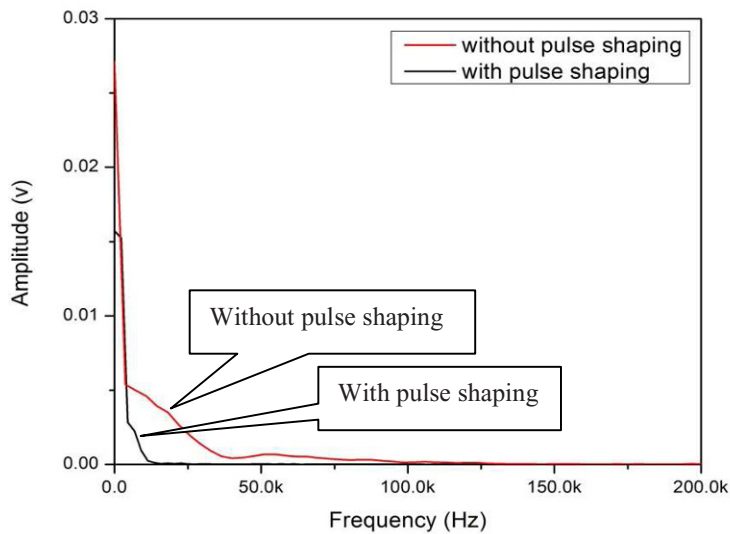


Figure 2.6 Frequency spectrums of the incident pulses produced without and with a pulse shaper

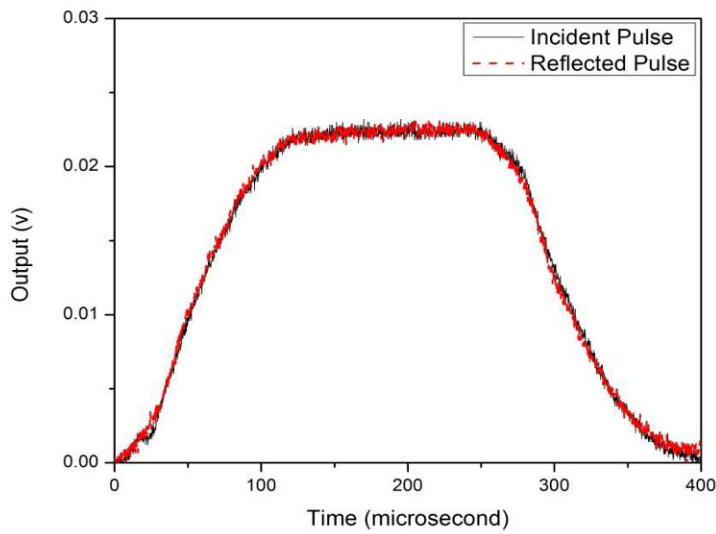


Figure 2.7 The incident and reflected pulses produced in a pulse-shaped Kolsky-bar experiment



## 2.2 Interfacial Friction

In a Kolsky-bar experiment, due to the short specimen required by dynamic stress equilibrium considerations, the interfacial friction between the specimen and the bar ends may lead the specimen to a three-dimensional stress state. The interfacial friction can significantly increase the measured strength in specimens with high lateral expansion because the friction limits the lateral expansion (Zenker and Clos 1998). For example, even a lubricant with a 0.05 friction coefficient produced an increase by 25% in the flow stress in a polyethylene specimen (Briscoe and Nosker 1984). Interfacial friction can also reduce the measured strength of brittle materials with small lateral expansion because the friction may result in multiaxial stress states at the specimen ends, causing premature failure.

Figure 2.8 shows a comparison of stress-strain curves for an alumina-filled epoxy without lubricant, with high vacuum grease and petroleum jelly as lubricants (Song et al. 2009c). All three stress-strain curves had similar elastic-perfectly plastic profiles with the same Young's modulus. However, the stress-strain curve without lubricant exhibits the highest apparent flow stress. Without lubricant, the interfacial friction restricted the specimen expansion laterally, which in turn increased the axial flow stress, particularly when the specimen is subject to large deformation. The elastic response was not significantly affected because the radial deformation in the specimen is relatively small during this stage. There is no significant difference in stress-strain response of the alumina-filled epoxy when using petroleum jelly or high vacuum grease as the lubricant.

Proper lubrication between the specimen and the bar interfaces is thus important. The lubricants may be different for different material characterization. Commonly used lubricants include high vacuum grease, petroleum jelly, polytetrafluoroethylene (PTFE), and molybdenum disulphide ( $\text{MoS}_2$ ) (Trautmann et al. 2005). Vegetable oil has been used when characterizing some specific specimen materials, such as biological tissues (Hall and Guden 2003, Pervin and Chen 2009).

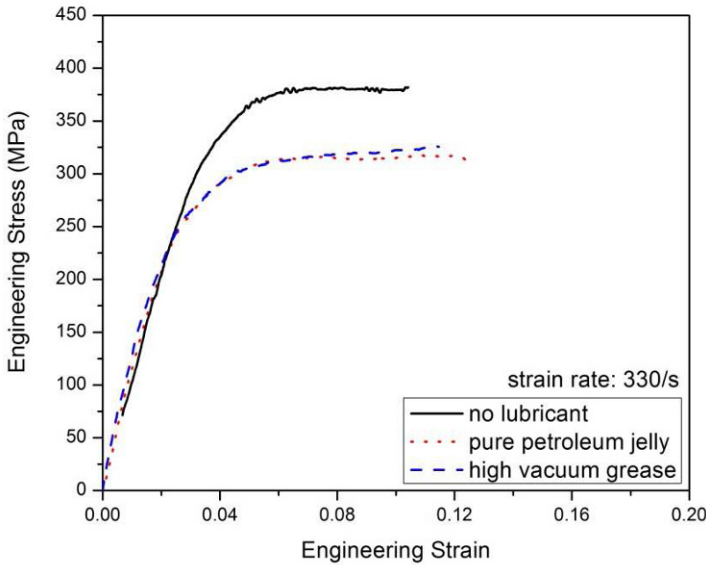


Figure 2.8 Lubrication effect on dynamic response of an alumina-filled epoxy  
(Reproduced from Song *et al.* (2009c) with permission)

## 2.3 Inertia Effects in Specimen

Inertia effects are associated with most dynamic events. In a Kolsky-bar experiment, the specimen is initially at rest and is expected to deform at a desired rate. Acceleration, and thus inertia in both axial and radial directions, accompanies the strain rate change from zero to the desired level. However, the goal of the Kolsky-bar experiments is to determine the intrinsic material response. Inertia effects should be minimized through appropriate design of specimen geometry and experimental conditions.

In the analysis of the inertia effects in the specimen for Kolsky-bar experiments, Samanta (1971) corrected a previous analysis with the addi-

tional consideration of the rate of change of specimen energy in the convective part. The specimen stress was measured by the mean value of stresses at both ends with additional inertia terms.

$$\sigma = -\frac{1}{2}(\sigma_1 + \sigma_2) - \rho_0 \left( \frac{l_0^2}{12} + \frac{a^2}{8} \right) \varepsilon - \rho \left( \frac{l_0^2}{12} - \frac{a^2}{16} \right) \varepsilon^2 \quad (2.4)$$

where  $\rho_0$  and  $\nu$  are density and Poisson's ratio of the specimen material, respectively;  $a$  is specimen radius; and  $\varepsilon$  is the time rate of change of strain rate in the specimen;  $\sigma_1$  and  $\sigma_2$  are the specimen stresses at the incident and transmission bar ends, respectively. Samanta's analysis indicates that the length-to-diameter ratio of  $\sqrt{3}/4$  and a constant strain rate should be satisfied simultaneously to eliminate the inertia effect. The benefit of stress equilibrium from constant strain rate has also been confirmed by Gorham (1989). Gorham (1989) modified the inertia component of stress as

$$\Delta\sigma = \sigma_2 - \sigma_1 = \rho \frac{h^2}{2} \varepsilon \quad (2.5)$$

The axial acceleration is accompanied by the inertia (or acceleration) in the radial direction due to Poisson's effect. This effect becomes more significant for volume incompressible materials. Radial inertia has been recognized to produce extra axial stress in specimen. This extra axial stress due to radial inertia becomes a significant concern when characterizing very soft materials.

Kolsky (1949) used an energy method to calculate the extra axial stress caused by the radial inertia,

$$\sigma = \frac{\nu^2 a^2 \rho_0}{2} \varepsilon \quad (2.6)$$

Forrestal et al. (2006) presented a closed-form solution of the extra axial stress due to radial inertia based on linear elasticity. For incompressible materials ( $\nu = 0.5$ ), the first order perturbation stress components at the radius of  $r$  in cylindrical coordinates are

$$\sigma_z = \sigma_\theta = \sigma_r = \frac{\rho_0 (a^2 - r^2)}{4} \varepsilon \quad (2.7)$$

The extra axial stress produced by radial inertia has a parabolic distribution, which suggests the maximum value of the extra axial stress at  $r = 0$  (specimen center) and zero at the specimen cylindrical surface ( $r = a$ ). The average extra axial stress over the entire specimen cross section is obtained from

$$\bar{\sigma}_z = \frac{1}{\pi a^2} \int_0^a \int_0^{2\pi} \sigma_z r dr d\theta \quad (2.8)$$

which has been found to be consistent with Kolsky's analysis (2.6). Both (2.6) and (2.7) indicate the radial inertia effect is eliminated when the specimen is subject to constant strain-rate deformation. It is noted that (2.6) is derived from linear elasticity, which is usually used for linear response at small deformation, such as brittle material response.

Warren and Forrestal (2010) extended the analysis of radial inertia effect to large plastic deformation, which benefits more engineering materials and biological tissues capable of large deformation. For a specimen undergoing large plastic deformation, the extra axial stress produced by radial inertia is

$$\sigma_z = \frac{\rho_0}{4(1-\varepsilon)^2} \left[ \frac{3\varepsilon^2}{2(1-\varepsilon)} + \varepsilon \right] (a_o^2 - r^2) \quad (2.9)$$

The extra stress induced by inertia and expressed by (2.9) also has a parabolic distribution in the radial direction. Similarly, the average axial stress, which is Cauchy stress, is

$$\bar{\sigma}_z = \frac{1}{\pi a^2} \int_0^a 2\pi \sigma_z r dr = \frac{3\rho_0 a_o^2}{16(1-\varepsilon)^3} \varepsilon^2 + \frac{\rho_0 a_o^2}{8(1-\varepsilon)^2} \varepsilon \quad (2.10)$$

Both strain and strain rate in (2.9) and (2.10) are in engineering measurements. In contrast to the linear elasticity analysis, the radial inertia will not be eliminated at large deformation even though the strain rate is constant. With increasing strains in the specimen, the radial inertia becomes more significant.

As indicated in (2.10), the amplitude of the extra axial stress produced by radial inertia depends on specimen density, radius, strain and strain rate. Within the strain rate range of Kolsky-bar experiment, the amplitude of the extra axial stress is approximately in the order of 1 MPa or below. Such a small amplitude is negligible for most engineering ma-

terials when the flow stress is on the order of  $10^2$  to  $10^3$  MPa. However, for very soft materials, such as soft rubbers, gelatins, and biological tissues, the stresses in which are often expressed in kPa, the radial inertia becomes a serious source of error. Since this radial inertia is not a part of the intrinsic material response of the specimen, it must be removed from experimental measurements. This issue will be further addressed in Chapter 4.2.

## 2.4 Constant Strain Rate Deformation

The Kolsky bar is designed to obtain families of stress-strain curves as a function of strain rate for the material under investigation. For each stress-strain curve, the strain rate is thus desired to be constant, particularly for those strain-rate-sensitive materials. As presented in the previous section, constant strain rate deformation also helps to validate the Kolsky bar testing conditions by minimizing inertia effects at small strains.

Unlike the quasi-static universal testing frames, the Kolsky-bar system is not sufficiently rigid in comparison to the specimen material. A constant velocity input, as generated in the form of the trapezoidal incident pulses in conventional Kolsky-bar experiments, does not necessarily produce constant-rate deformation in the specimen. [Figure 2.9](#) illustrates typical strain-rate histories in an elastic-brittle and an elastic-plastic specimen from conventional Kolsky-bar experiments. Both strain rates are observed far from constant, particularly for the elastic brittle specimen. For a work-hardening material, the input stress level needs to progressively increase to deform the specimen at a constant rate. Otherwise, the engineering strain rate in the specimen decreases. The generation of an incident pulse with increasing amplitude in a Kolsky-bar experiment is an open loop control over the testing conditions on the specimen. Such control is a part of the Kolsky-bar experiment design.

Since the impact experiment does not allow real-time adjustment on the loading pulse based on the specimen feedback, the adjustment process on the control to achieve desired testing conditions on the specimen is iterative. In most cases, the conventional trapezoidal type of incident pulse does not satisfy the requirement of constant strain-rate deformation. However, the transmitted pulse from such a conventional experiment reveals information about the specimen response. Based on this response, the incident pulse is modified in the next experiment in order to

approach dynamic equilibrium and constant strain rate. The method to modify the incident pulse is pulse shaping technique.

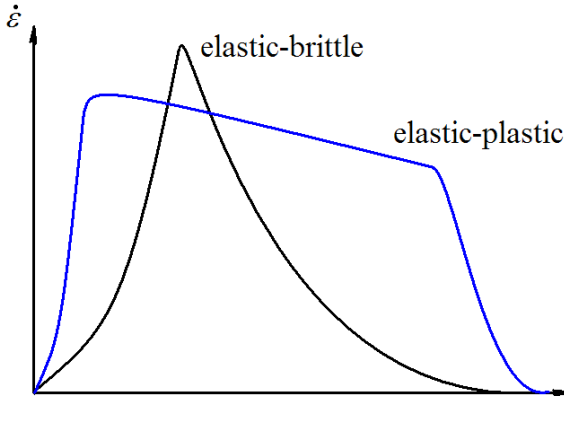


Figure 2.9 Illustration of strain rate histories for elastic-brittle and elastic-plastic materials in conventional Kolsky-bar experiments

## 2.5 Pulse Shaping Technique

Pulse shaping technique is used to facilitate stress equilibrium and constant strain rate deformation in the specimen through properly modifying the profile of the incident pulse based on specimen response in Kolsky-bar experiments.

Pulse shaping technique has been discussed and developed over the past three decades. Duffy et al. (1971) were probably the first authors to use pulse shapers to smooth pulses generated by explosive loading for the torsional Kolsky bar. Christensen et al. (1972) might be the first au-

thors to employ a pulse shaping technique in the compression version of Kolsky-bar tests to improve the accuracy and resolution of the initial portions of the stress-strain curves. They modified the incident pulse with a pulse shaping technique in Kolsky-bar experiments on rocks. A ramp incident pulse was found to be more appropriate than a square pulse in Kolsky bar experiments to obtain accurate compressive stress-strain response for rocks. In their study, they used conical strikers instead of the usual cylinders to partially accomplish ramp-like incident loading pulse. It is noted that the small end of the cone was fired as the impact end. The generated profile of the incident pulse corresponds to three loading regions: the initial impact of the truncated cone, the transition region determined by the cone angle, and the final region depending on the area of the cylinder joined to the cone. The profile of the input-stress wave can be varied over a considerable range with this technique through varying the area ratio of the cylinder and the cone, as shown in Fig. 2.10. A conical striker for pulse shaping technique is still being used for Kolsky-bar experiments on brittle materials (Lok et al. 2002). Figure 2.11 shows a schematic of currently used conical striker. Although the profile of incident pulse can be modified by varying the geometry of the striker, it brings difficulties to design and fabricate the specialized striker.

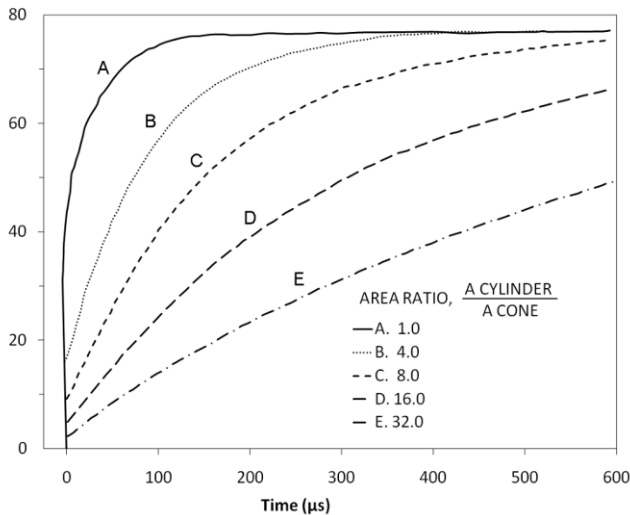


Figure 2.10 Incident pulses produced by varying the area ratio between the cylinder and the cone  
(Reproduced from Christensen et al. (1972) with permission)

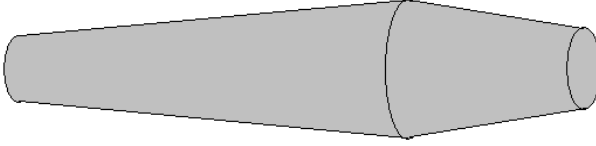


Figure 2.11 Schematic of conical striker

In order to facilitate constant strain-rate deformation in specimen, the incident pulse is generally required to possess a similar profile to the stress response of the tested specimen, which is represented by the transmitted signal. A three-bar technique for pulse shaping was developed to achieve this goal. [Figure 2.12](#) illustrates the design of the three-bar technique (Ellwood et al. 1982). An additional pressure bar (preloading bar) and dummy specimen were implemented to the conventional Kolsky-bar configuration. The dummy specimen is recommended to be made of the same material as the tested specimen. The pulse transmitted through the dummy specimen becomes the actual incident pulse for the real specimen. Under this arrangement, the profile of the incident pulse is very similar to that of the transmitted pulse measured behind the specimen. This incident pulse produces a plateau in the reflected pulse, representing a constant strain rate in the specimen. [Figure 2.13](#) shows typical incident, reflected, and transmitted pulses produced from the three-bar technique (Ellwood et al. 1982). The incident pulse was dictated by the dummy specimen's elastic-plastic response. This elastic-plastic response is very similar to that for the actual specimen because they are made of the same material. The actual specimen was thus subjected to a nearly constant strain-rate deformation, as indicated by the plateau in the reflected pulse in [Fig. 2.13](#).



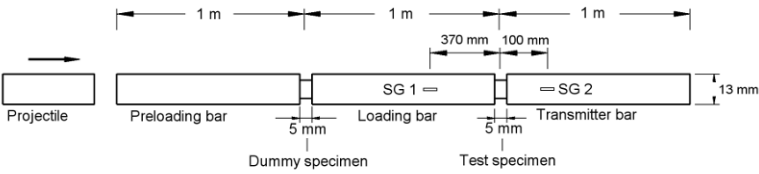


Figure 2.12 Three-bar technique  
(Reproduced from Ellwood et al. (1982) with permission)

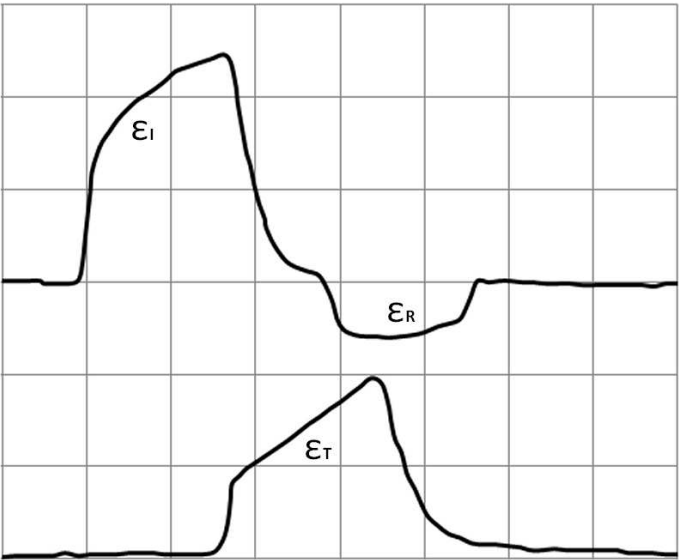


Figure 2.13 Pulse shaped Kolsky bar experiment  
with the three-bar technique  
(Reproduced from Ellwood et al. (1982) with permission)

The preloading bar in the three-bar technique was made from the same material as the incident and transmission bars. However, Parry et al. (1995) replaced the preloading bar with a lower-strength bar to minimize the stress wave dispersion. The reduction of the wave dispersion depends on the length of the pre-loading bar. A longer pre-loading bar minimizes the wave dispersion more efficiently.

As a simpler version of the three-bar technique, the pre-loading bar was removed. The dummy specimen was directly placed at the end of the incident bar and is subjected to the direct impact of the striker (Bragov and Lomunov 1995). Another alternative for controlling the incident pulse profile is to place a “tip” material between the striker and the incident bar, as illustrated in [Figure 2.14](#). The tip material is usually called “pulse shaper” in Kolsky-bar experiments. The function of the pulse shaper in Kolsky-bar experiments includes minimizing wave dispersion, facilitating stress equilibrium and constant strain rate deformation in specimen.

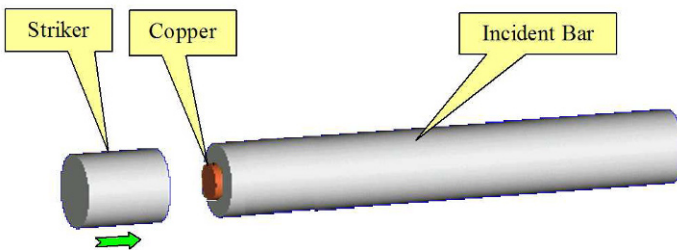


Figure 2.14 Pulse shaping technique with a copper “tip” material

This “tip” material is not necessarily the same as the specimen material under investigation. The tip material is commonly a disc made from paper, aluminum, copper, brass, stainless steel, and so on. Annealed copper discs have recently been extensively used as pulse shapers in Kolsky-bar experiments. Nemat-Nasser et al. (1991) might be the first authors to analytically model the pulse-shaping process using OFHC (oxygen-free, high-purity copper) as pulse shaper. Their analysis is based on the following constitutive response,

$$\sigma_c = \sigma_0 f(\varepsilon) \quad (2.11)$$

where the function  $f(\varepsilon)$  is determined experimentally,  $\sigma_0$  is a constant although it may depend on the strain rate in general. In (2.11),  $\sigma_c$  refers to true stress; whereas,  $\varepsilon$  is engineering strain. If the copper pulse shaper has an initial area  $A_i$  and a thickness  $h_0$ , the axial strain  $\varepsilon$  in the pulse shaper as a function of time  $t$  can be calculated with

$$\left( \frac{h_0}{V_0} \right) \varepsilon + K \frac{f(\varepsilon)}{1 - \varepsilon} = 1 \quad (2.12)$$

where

$$K \equiv \frac{A_i \sigma_0}{A_b \sigma_m} \quad (2.13)$$

$$\sigma_m \equiv \frac{1}{2} \rho_b C_b V_0 \equiv \frac{1}{2} \frac{E_b}{C_b} V_0. \quad (2.14)$$

Equation (2.12) has the solution

$$t = \int_0^\varepsilon \left[ 1 - K \frac{f(x)}{1 - x} \right]^{-1} dx \quad t \leq T \quad (2.15)$$

$T$  is defined by (1.1). The strain and stress in the incident bar,  $\varepsilon_b$  and  $\sigma_b$ , are

$$\varepsilon_b = \frac{A_1 \sigma_0}{A_b E_b} \cdot \frac{f(\varepsilon)}{1 - \varepsilon} \quad (2.16)$$

$$\sigma = E_b \varepsilon_b \quad (2.17)$$

Assuming unloading of the pulse shaper occurs at  $t = T_1$ , the strain of the pulse shaper at  $T \leq t \leq T_1$  is determined by integrating the following strain rate history,

$$\varepsilon(t) = \frac{V_0}{h_0} \left\{ 1 - K \left[ \frac{f(\varepsilon(t))}{1 - \varepsilon(t)} + \frac{f(\varepsilon(t - t_0))}{1 - \varepsilon(t - t_0)} \right] \right\}, \quad T \leq t \leq T_1 \quad (2.18)$$

The strain and stress produced in the incident bar are then determined with (2.16) and (2.17), respectively.

Frew et al. (2002) presented a more extensive analysis to determine the strain of the pulse shaper. The pulse shaper deformation was derived as

$$\frac{h_0}{V_0} \varepsilon(t) = 1 - K' \left( \frac{1}{\rho_b C_b} + \frac{1}{\rho_{st} C_{st}} \right) \frac{f(\varepsilon)}{1 - \varepsilon}, \quad \text{for } 0 \leq t < T \quad (2.19)$$

$$\frac{h_0}{V_0} \varepsilon(t) = 1 - K' \left( \frac{1}{\rho_b C_b} + \frac{1}{\rho_{st} C_{st}} \right) \frac{f(\varepsilon)}{1 - \varepsilon} - \frac{2K'}{\rho_{st} C_{st}} \sum_{k=1}^n \frac{f(\varepsilon(t - kT))}{1 - \varepsilon(t - kT)},$$

$$\text{for } nT \leq t < (n+1)T \quad (2.20)$$

where

$$K' = \frac{\sigma_0 A_1}{A V_0} \quad (2.21)$$

Equations (2.19) and (2.20) have the following solutions, respectively.

$$t = \frac{h_0}{V_0} \int_0^\varepsilon \left[ 1 - K' \left( \frac{1}{\rho_b C_b} + \frac{1}{\rho_{st} C_{st}} \right) \frac{f(x)}{(1-x)} \right]^{-1} dx, \quad \text{for } 0 \leq t < T \quad (2.22)$$

$$t = nT + \frac{h_0}{V_0} \int_0^{\varepsilon^n} \left[ 1 - K' \left( \frac{1}{\rho_b C_b} + \frac{1}{\rho_{st} C_{st}} \right) \frac{f(x)}{(1-x)} - \frac{2K'}{\rho_{st} C_{st}} \sum_{k=1}^n \frac{f(\varepsilon(t-kT))}{1-\varepsilon(t-kT)} \right]^{-1} dx$$

for  $nT \leq t < (n+1)T$  (2.23)

where  $\varepsilon^n$  is the strain in the pulse shaper at  $t = nT$ . The strain in the incident bar can be obtained from (2.16) after the pulse shaper strain is calculated from (2.22) and (2.23). Equations (2.22) and (2.23) are valid as long as the pulse shaper does not expand beyond the bar surfaces. The unloading response of the pulse shaper was also analyzed by Frew et al. (2002). As a practical reference in Kolsky-bar experiment design, a FORTRAN source code for the numerical solution of the pulse shaping equations is attached in Appendix A of this book, which was provided by Dr. Frew.

Using such a code, the shapes of the incident pulses can be predicted on the computer before pulse shapers are made, which improves the efficiency of the high-rate experiment design. As an example, if an annealed copper is used as the pulse shaper, its stress-strain response has been determined to have the following form,

$$\sigma_p = \frac{\sigma_0 \varepsilon_p^n}{1 - \varepsilon_p^m} \quad (2.24)$$

By curve fitting to experimental results on the pulse shaper material, the constants  $\sigma_0$ ,  $n$ , and  $m$  are determined. Then the incident stress (or strain) histories can be predicted by the pulse-shaping models. Figure 2.15 shows experimental data and model predictions for incident stresses from a pulse shaped experiment with an annealed C11000 copper pulse shaper and Frew's model (Frew et al. 2002).

When a high-strength elastic-plastic material is to be characterized by the Kolsky-bar experiments with pulse shaping, the soft copper pulse shaper may not produce the desired incident pulse because of its low yield strength. In this case, a harder pulse shaper is necessary. However, the harder pulse shaper usually generates a high rate of loading even during initial loading stage, which is not desired for achieving early stress equilibrium. Stacking the soft and hard pulse shapers together forms dual pulse shaping technique that is illustrated in Fig. 2.16. The dual pulse shaper consists of a softer material, such as a copper, and a relatively harder material such as a steel. During the initial compression, the de-

formation of the soft shaper is much larger than that of the hard one. It is highly possible that the cross section of the soft shaper is beyond the hard shaper. In this case, a very rigid platen with a large diameter is placed between the soft and hard pulse shapers such that the soft shaper can continue to flow to larger strains. The major role of the soft pulse shaper is to produce a relatively low initial rate of loading so that the stress equilibrium is achieved early during an experiment. When the soft pulse shaper is compressed to very large strains, it eventually tends not to be further compressible. The hard pulse shaper starts to dominate the shape of incident pulse from this moment. The hard pulse shaper generates the majority of the incident pulse so that a constant strain rate is achievable.

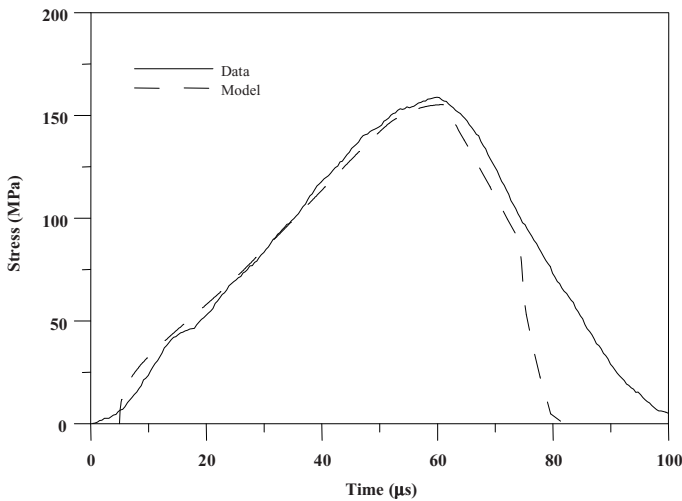


Figure 2.15 Incident pulse produced with annealed copper as pulse shaper  
(Reproduced from Frew et al. (2002) with permission)

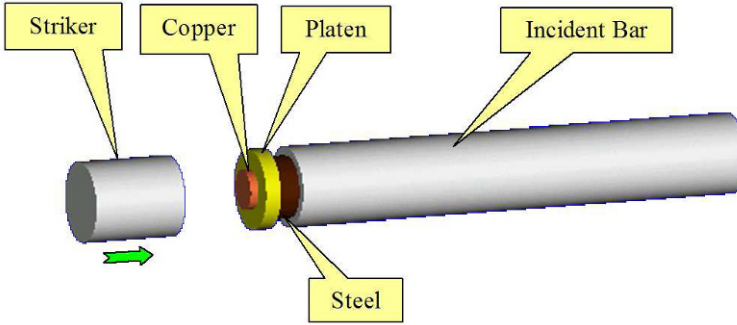


Figure 2.16 Dual pulse shaping technique

The dual pulse shaping technique for elastic-plastic material characterization has also been modeled by Frew et al. (2005). Both pulse shapers are assumed to have similar stress-strain response,

$$\sigma_{\alpha} = \sigma_{0\alpha} f(\varepsilon_{\alpha}) \quad (2.25)$$

$$\sigma_{\beta} = \sigma_{0\beta} g(\varepsilon_{\beta}) \quad (2.26)$$

where subscripts,  $\alpha$  and  $\beta$ , refer to the soft and hard pulse shaper, respectively. The responses of both pulse shapers are correlated during compression,

$$\frac{g(\varepsilon_{\beta})}{1 - \varepsilon_{\beta}} = \frac{a_{0\alpha}}{a_{0\beta}} \cdot \frac{\sigma_{0\alpha} f(\varepsilon_{\alpha})}{\sigma_{0\beta} (1 - \varepsilon_{\alpha})} \quad (2.27)$$

Very similar to the single pulse shaping analysis, the deformation of dual pulse shapers is determined by

$$\frac{h_{0\alpha}}{V_0} \varepsilon_\alpha(t) = 1 - K'_\alpha \left[ \frac{1}{\rho_b C_b} + \frac{1}{\rho_{st} C_{st}} \right] \frac{f(\varepsilon_\alpha)}{1 - \varepsilon_\alpha} - \frac{h_{0\beta}}{V_0} \varepsilon_\beta(t), \text{ for } 0 \leq t < T \quad (2.28)$$

$$\begin{aligned} \frac{h_{0\alpha}}{V_0} \varepsilon_\alpha(t) = & 1 - K'_\alpha \left[ \frac{1}{\rho_b C_b} + \frac{1}{\rho_{st} C_{st}} \right] \frac{f[\varepsilon_\alpha(t)]}{1 - \varepsilon_\alpha(t)} \\ & - \frac{2K'_\alpha}{\rho_{st} C_{st}} \left\{ \frac{f[\varepsilon_\alpha(t-T)]}{1 - \varepsilon_\alpha(t-T)} + \frac{f[\varepsilon_\alpha(t-2T)]}{1 - \varepsilon_\alpha(t-2T)} \right. \\ & + \left. \frac{f[\varepsilon_\alpha(t-nT)]}{1 - \varepsilon_\alpha(t-nT)} \right\} - \frac{h_{0\beta}}{V_0} \varepsilon_\beta(t) \\ & \text{for } nT \leq t < (n+1)T \end{aligned} \quad (2.29)$$

where

$$K'_\alpha = \frac{\sigma_{0\alpha} a_{0\alpha}}{A_b V_0} \quad (2.30)$$

Equations (2.28) and (2.29) are valid only when the pulse shapers remain in compression and do not expand beyond the cross sections of the striker and incident bar. It is obvious that the dual pulse shaper model is more complicated than the single pulse shaper model. The response of both pulse shapers are coupled together, which requires numerical solutions to the combination of (2.27), (2.28) and (2.29). [Figure 2.17](#) shows an example of the dual pulse shaper modeling and corresponding data from an experiment by using annealed C11000 copper ( $\alpha$ ) and a 4340 Rc35 steel ( $\beta$ ) as the pulse shapers (Frew et al. 2005). The detailed application of the dual pulse shaping technique is presented in Chapter 5.

Depending on the desired testing conditions on the specimens under investigation, the generation of incident pulse can be very diverse by varying the material, geometry, and dimensions of the pulse shaper(s) as well as the striking velocity, material, and geometry of the striker. [Figure 2.18](#) shows a few dimensionless incident pulses generated with various pulse shaping designs (Chen and Song 2009). These pulses are designed for characterizing the materials with different characteristics in stress-strain response, in order to facilitate constant strain-rate deformation un-



der stress equilibrium. Detailed pulse shaping techniques for different material characterization is presented in the next several chapters. It is also noted that this solution of the pulse shaping design is not exclusive. Any design is acceptable as long as it produces an incident pulse that satisfies the requirements of constant strain rate deformation and stress equilibrium.

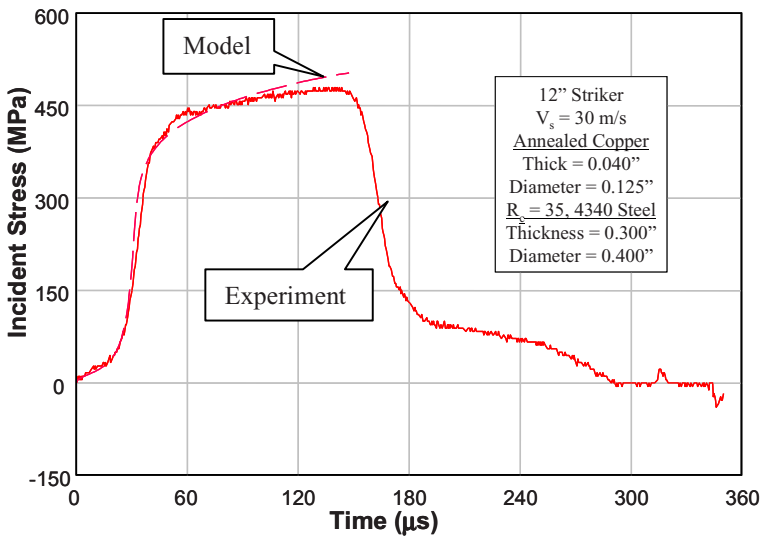


Figure 2.17 Incident pulse produced with dual pulse shaping technique  
*(Reproduced from Frew et al. (2005) with permission)*

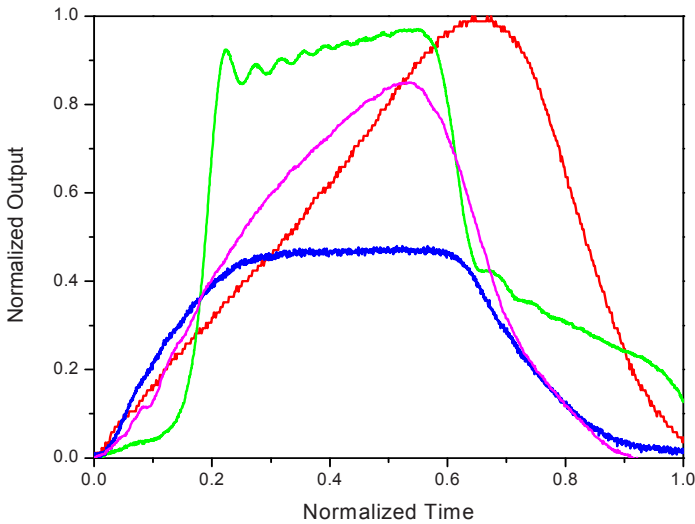


Figure 2.18 Various incident pulses produced with different pulse shaping designs  
(Reproduced from Chen and Song (2009) with permission)

## 2.6 Single Loading and Unloading Control

When the striker impacts on the incident bar, the resulting stress wave propagates back and forth within the Kolsky-bar system. Figure 2.19 illustrates the stress waves measured with the strain gages in the middle of the incident bar in a typical Kolsky bar experiment. The corresponding displacement history of the incident bar end is also illustrated in Fig. 2.19. Figure 2.19 indicates that every time the stress wave reflects back from the specimen side, the bar end moves a small step. The stop-and-go response of the incident bar end has the specimen compressed progressively. Usually only the pulses associated with the first loading are recorded to calculate the stress-strain response of the specimen material; however, the specimen recovered after the experiment was actually subjected to multiple loading in a single Kolsky bar experiment. This causes

confusion in any attempt to correlate the mechanical response of the specimen with its microstructural change. If such correlation between the loading history and the microstructure evolution is desired, the specimen should be subjected to only a single loading. In other words, only the first loading goes through the specimen while the additional momentum after the first loading is trapped.

The concept of momentum trapping in Kolsky-bar experiments appeared as early as 1960s (Baker and Yew 1966), but different designs have been developed recently.

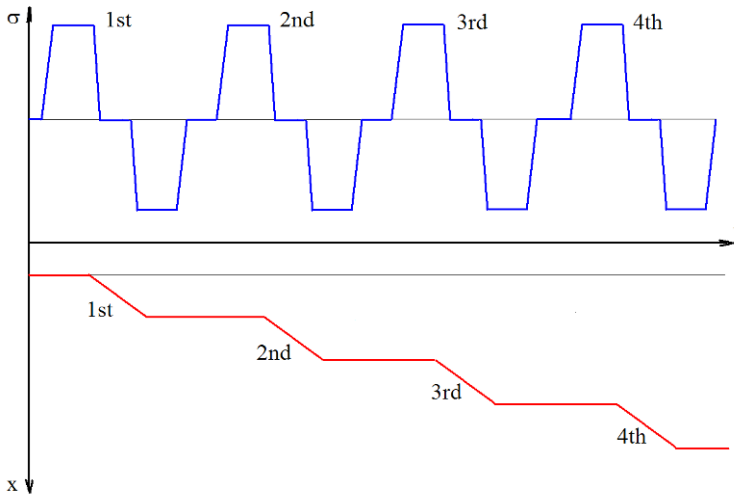


Figure 2.19 Multiple loading in Kolsky-bar experiment

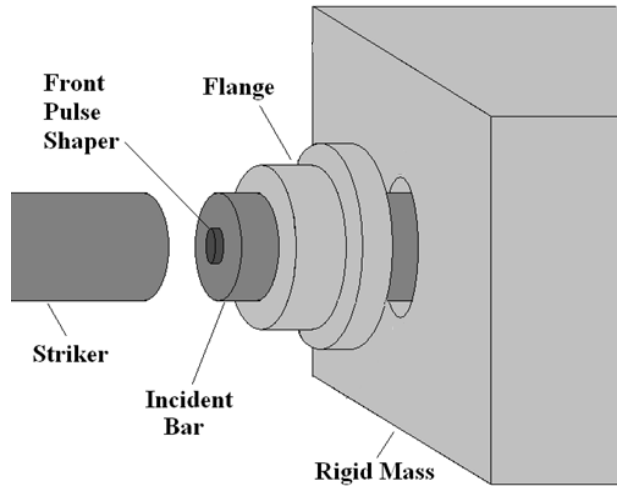


Figure 2.20 Modified momentum trap for Kolsky compression bar  
(Reproduced from Song and Chen (2004c) with permission)

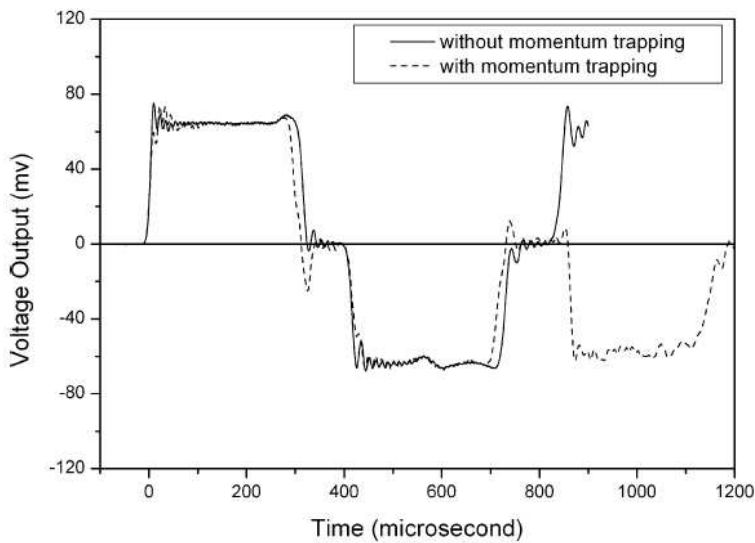


Figure 2.21 Comparison of pulses obtained with and without the momentum trap  
(Reproduced from Song et al. (2006c) with permission)

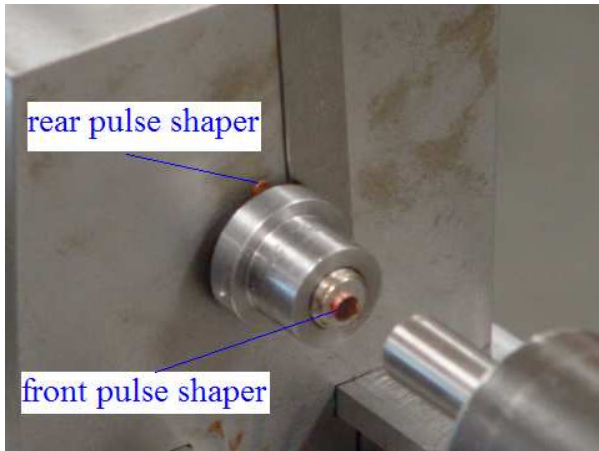


Figure 2.22 Rear pulse shaping technique

Song and Chen (2004c) modified a momentum trap concept and developed a single loading device for Kolsky compression bar which is illustrated in Fig. 2.20. As shown in Fig. 2.20, this momentum trap consists of a rigid mass and a flange attached to the impact end of the incident bar. The incident bar passes through the rigid mass that plays a role to trap the momentum (stop the bar system) after first impact. There exists a gap between the flange and the rigid mass that needs to be preset precisely. The necessary width of the preset gap,  $d$ , is determined with the incident strain history,

$$d = C_0 \int_0^T \epsilon_I(t) dt \quad (2.31)$$

This gap allows only the first compressive pulse to pass into the incident bar before it is closed. The reaction mass then plays a role of rigid wall to block the incident bar from any further movement so that no more compression is loaded on the specimen. Figure 2.21 shows a comparison of the pulses with and without the momentum trap (Song et al. 2006c). It clearly shows that the secondary compression in the experiment without momentum trap is turned into a tensile pulse that pulls the incident bar back from the specimen when the single loading system is employed.

This new design of the momentum trap does not affect the application of the pulse shaping technique. Rather, it provides possibility of controlling not only the loading portion of the incident pulse but also the unloading portion through a reverse pulse shaping technique. The pulse shaping technique described so far in the book is to place the pulse shaper(s) on the impact surface of the incident bar to control the profile of the incident pulse. In this manner, only the loading portion is controllable. The unloading portion remains to be uncontrolled, which is not acceptable when the unloading cannot be random in the characterization of certain materials. For some materials with unique hysteretic stress-strain response such as shape memory alloys and viscoelastic or viscoplastic solids, it is desirable to understand their stress-strain response not only for loading but also for unloading. In some cases, understanding unloading stress-strain response is even more important than loading response. In order to obtain a valid loading-unloading stress-strain loop, the strain rate should be the same constant for both loading and unloading. The entire profile of the incident pulse including both loading and unloading needs to be under control.

The loading profile is controlled with the conventional pulse shaping technique while the unloading part is controlled through the reverse pulse shaping where pulse shapers are placed between the flange and reaction mass, as shown in Fig. 2.22. The rear pulse-shapers placed on the surface of the rigid mass initially has a preset gap from the flange. During an experiment, the front pulse-shaper is extensively compressed at first, generating a desired incident loading profile that deforms the specimen at a constant strain rate under dynamic stress equilibrium over the loading phase of the experiment. The gap between the flange and the rigid mass is then closed. The rear pulse-shapers on the surface of the rigid mass are thereafter compressed by the flange, changing the unloading profile of the incident pulse. This controlled unloading profile in the incident pulse ensures that the specimen recovers at the same constant strain rate during unloading. A compressive stress-strain hysteretic response for the material is thus obtained at a certain constant rate of both loading and unloading. The detailed applications of this technique are discussed in Chapters 4.5.1 (for PMMA) and 5.3.2 (for shape memory alloy).

The above momentum trap was designed following the general concept of the stress reversal Kolsky bar that was developed by Nemat-Nasser et al. (1991). The overall design of their setup is shown in Fig. 2.23. In addition to the conventional Kolsky-bar design, a transfer flange, a tube over the bar, and a reaction mass were implemented (Fig. 2.23). The incident tube is placed against the transfer flange at one end and against the reaction mass at the other end. When the striker impacts the

transfer flange, it imparts two common compression pulses traveling along the incident tube towards the reaction mass and along the incident bar towards the specimen. The compressive pulse in the incident tube is reflected from the reaction mass and travels back to the transfer flange also as compression. The compression is reflected from the flange as tension. This tension makes the particle velocity in the incident bar move in the reverse direction, avoiding the second compression on the specimen. The resultant incident pulse is thus a combination of compression-tension, as shown in Fig. 2.24 (Nemat-Nasser et al. 1991)

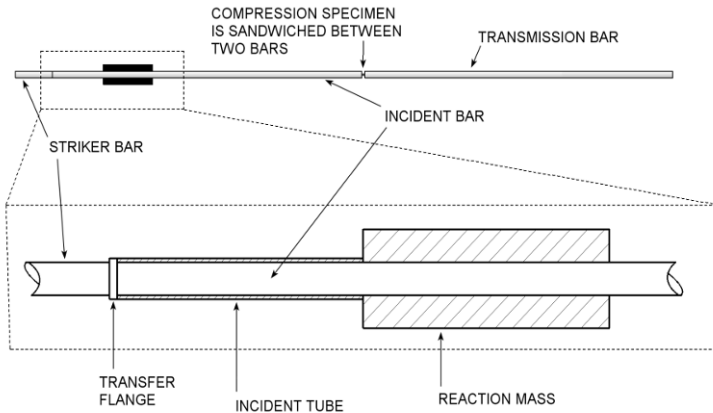


Figure 2.23 Stress reversal Kolsky bar  
(Reproduced from Nemat-Nasser et al. (1991) with permission)

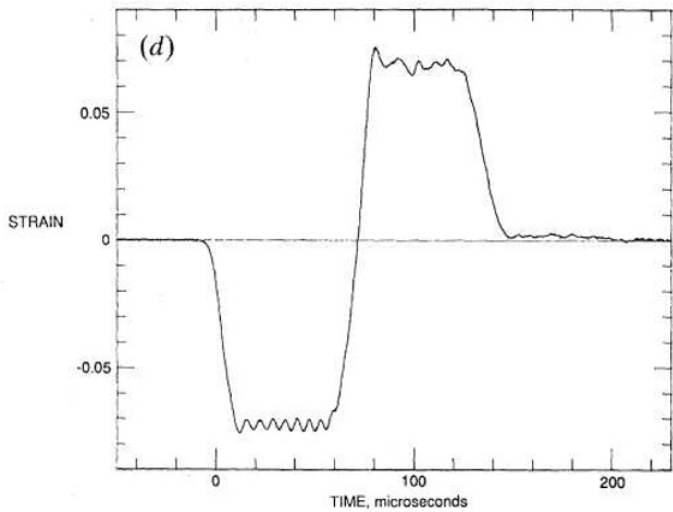


Figure 2.24 Incident pulse generated with the stress reversal Kolsky bar  
(Reproduced from Nemat-Nasser et al. (1991) with permission)

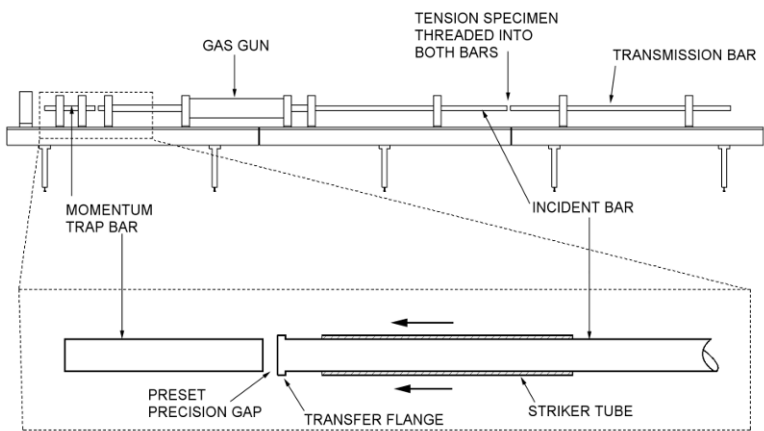


Figure 2.25 Momentum trapped Kolsky tension bar  
(Reproduced from Nemat-Nasser et al. (1991) with permission)



Due to the additional incident tube, part of the external impact load is distributed to the incident tube, which is then reversed. This excessive stress may overwhelm the flange root when high stress levels are required for hard material characterization.

The momentum trap has also been developed for Kolsky tension bar with a very similar mechanism, as shown in [Fig. 2.25](#) (Nemat-Nasser et al. 1991). A momentum trap bar is set aside the transfer flange on the incident bar with a preset gap. The gap needs to be precisely set such that the momentum trap bar starts to be in contact with the transfer flange surface once the first tensile pulse transfers into the incident bar through the transfer flange. The tensile pulse in the incident bar is reflected back at the incident bar/specimen interface, becoming compression. Without the momentum trap bar or with a wider gap between the momentum trap bar and the transfer flange, the compressive pulse turns back to the incident bar as the secondary tensile pulse, pulling the specimen in tensile deformation again. However, with the precisely preset gap between the momentum trap bar and the transfer flange, the compressive pulse directly transmits into the momentum trap bar, which will be reflected back at the far free end as a tensile pulse. This tensile pulse pulls the momentum trap bar off the incident bar as the contact interface with the transfer flange does not support tension. The pulse is thus trapped within the momentum trap bar; whereas, the incident bar remains at rest. Consequently the specimen is subject to only the first tensile loading.

## 2.7 Upper Limit of Strain Rate

In Kolsky-bar experiments for material property characterization, dynamic stress equilibrium and constant strain rate need to be achieved in the specimen. Since the specimen is initially at rest, the ideal testing conditions are not satisfied over the entire duration of the experiment. It takes time for the stress waves to bring the specimen into near equilibrium and the strain rate to a desired constant level. If the desired strain rate is very high, the specimen may fail as the strain rate is still rising. Therefore, there is a limit for the maximum strain rate for achieving dynamic stress equilibrium and constant strain rate simultaneously. Beyond this upper limit of strain rate, the specimen may deform under neither equilibrated stress nor constant strain rate. To estimate the validity range of the experimental results, it is necessary to know the upper limit

of strain rates that corresponds to certain strains where the material response drastically changes, such as plastic yielding or failure.

As mentioned earlier, stress wave takes several rounds of reflections back and forth in the specimen to approximately achieve dynamic stress equilibrium. The number of reflections required for dynamic stress equilibrium varies for different materials and different loading conditions. If we assume the required number of reflections is  $n$ , the corresponding time for the specimen to achieve stress equilibrium is

$$t = n \frac{L_s}{C_s} \quad (2.32)$$

If the specimen deforms at a constant strain rate, the strain accumulated before the specimen is in equilibrium is

$$\varepsilon = \dot{\varepsilon} \cdot t = n \dot{\varepsilon} \frac{L_s}{C_s} \quad (2.33)$$

In order to ensure the validity of the resultant data, any critical event, for example, either plastic yielding or failure, should not occur prior to this accumulated strain,

$$\varepsilon < \varepsilon_{cr} \quad (2.34)$$

where  $\varepsilon_{cr}$  is the critical strain for such an event. Hence, the strain rate is limited due to the requirement of stress equilibrium (Ravichandran and Subhash 1994),

$$\dot{\varepsilon} < \frac{\varepsilon_{cr} C_s}{n L_s} \quad (2.35)$$

The above strain-rate limit is derived from consideration of stress equilibrium. Another requirement is the achievement of constant strain rate, which turns out to be a more restrictive limit. In Kolsky-bar experiments, the strain rate has to increase from zero to a targeted value. It takes a finite amount of time for this process to take place, while the strain in the specimen is being accumulated. If the specimen fails or plastically yields during this process, the strain rate in the specimen during the entire loading process is not constant. Therefore, depending on the

failure strain in the specimen material, there is a limit on the achievable constant strain rate in the experiment.

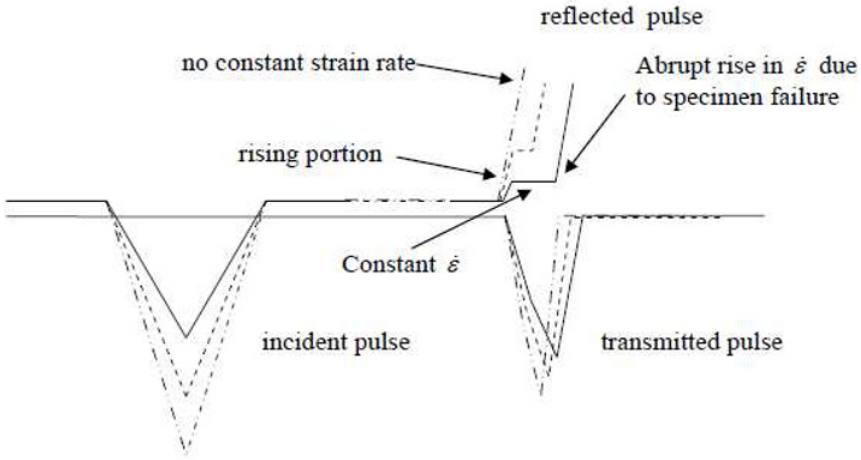


Figure 2.26 A schematic illustration of the upper limit of constant strain rate in a brittle specimen  
(Reproduced from Pan et al. (2005) with permission)

Figure 2.26 illustrates the upper limit of constant strain rate in a brittle specimen (Pan et al. 2005). As will be discussed in detail in Chapter 3, it is necessary to generate a linear stress pulse to achieve a constant strain rate in a linear and brittle specimen,

$$\sigma_i = M \cdot t \quad (2.36)$$

where  $M$  is the loading rate of such a linear (ramp) pulse. The strain-rate history in the linear specimen,  $\dot{\epsilon}_s$ , can be analytically estimated by (Frew et al. 2002)

$$\varepsilon_S = \frac{A_B}{A_S} \cdot \frac{M}{E_S} \left[ 1 - \exp \left( - \frac{2C_S t}{L_S} \cdot \frac{\rho_S C_S A_S}{\rho_B C_B A_B} \right) \right] \quad (2.37)$$

The strain history is calculated by integrating (2.37) with respect to time,

$$\varepsilon_S = \frac{A_B}{A_S} \cdot \frac{M}{E_S} \left\{ t - \frac{A_B L_S}{2 A_S C_S} \left[ 1 - \exp \left( - \frac{2C_S t}{L_S} \cdot \frac{\rho_S C_S A_S}{\rho_B C_B A_B} \right) \right] \right\} \quad (2.38)$$

The strain rate can be considered to be a constant from the instant  $t = \tau$  until the specimen fails. The instant,  $\tau$ , is determined by satisfying the following condition,

$$\xi = \left[ \exp \left( - \frac{2C_S t}{L_S} \cdot \frac{\rho_S C_S A_S}{\rho_B C_B A_B} \right) \right] \Big|_{t=\tau} \rightarrow 0 \quad (2.39)$$

Hence,

$$\varepsilon_S = \frac{A_B}{A_S} \cdot \frac{M}{E_S} \eta \quad (2.40)$$

where

$$\eta = 1 - \xi \quad (2.41)$$

For a brittle material, a constant strain rate needs to be achieved prior to specimen failure or any other significant events under investigation,

$$\varepsilon_S \Big|_{t=\tau} < \varepsilon_{cr} \quad (2.42)$$

or we have

$$\varepsilon_S < \frac{\beta}{\tau} \cdot \frac{\varepsilon_{cr}}{\alpha/\eta - 1} \quad (2.43)$$

where

$$\beta = \frac{2\tau C_S}{L_S} \cdot \frac{\rho_S C_S A_S}{\rho_B C_B A_B} \quad (2.44)$$

Hence, the upper limit of strain rate can be estimated with (2.43) for the consideration of constant strain-rate deformation.

Figures 2.27 and 2.28 show the strain rate histories from the pulse-shaped Kolsky-bar experiments on an S-2 glass/SC15 epoxy composite and a PMMA, respectively (Pan et al. 2005). In both figures, the solid dots indicate where the specimen starts to fail. The strain rate histories show that the critical strain rate for the composite is  $1700 \text{ s}^{-1}$ , beyond which non-constant strain rate is observed for the entire loading duration. When the desired strain rate is higher than  $1700 \text{ s}^{-1}$ , the specimen fails before a constant strain rate is achieved. In a very similar way, such a critical strain rate locates between  $1910$  and  $2130 \text{ s}^{-1}$  for the PMMA, as shown in Fig. 2.28. Table 2.1 presents a comparison of the upper strain-rate limit from theoretical estimates with (2.43) and experimental results for both materials, the result of which shows good agreement.

When estimating the upper limit of strain rate in Kolsky-bar experiments, both criteria of stress equilibrium and constant strain rate need to be satisfied simultaneously. The eventual upper limit of strain rate should be the minimum between the estimates from (2.35) and (2.43),

$$\varepsilon_{cr} = \min \left\{ \frac{\varepsilon_{cr} C_S}{\alpha L_S}, \frac{\beta \varepsilon_{cr}}{\tau(\beta/\eta - 1)} \right\} \quad (2.45)$$

Using the above materials as examples again, the upper limits of strain rate for the composite and PMMA are estimated with (2.35) for dynamic stress equilibrium as  $3950$  and  $9567 \text{ s}^{-1}$ , respectively. These limits are much higher than those tabulated in Table 2.1 that are estimated from constant strain rate consideration. This indicates the requirement of constant strain-rate deformation is more restrictive than stress equilibrium requirement when estimating the upper limit of strain rates in Kolsky-bar experiments.

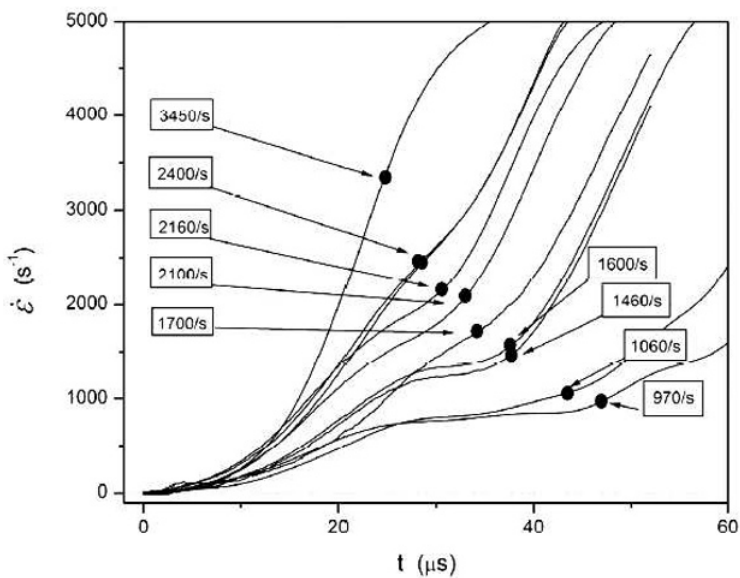


Figure 2.27 Strain-rate histories in composite specimens  
(Reproduced from Pan et al. (2005) with permission)

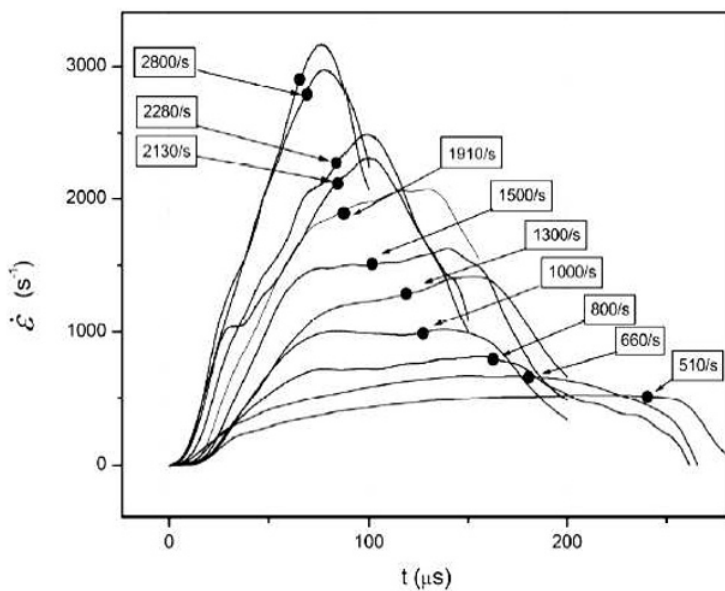


Figure 2.28 Strain-rate histories in PMMA specimen  
(Reproduced from Pan et al. (2005) with permission)

Table 2.1 Comparison of upper strain-rate limit  
from theoretical estimates and experimental results (Pan et al. 2005)

	PMMA	S-2 Glass/SC15 composite (in plane direction)
Theoretical estimate	1735 /s	1499 /s
experiments	~1910 /s	1600/s~1700 /s

Split Hopkinson (Kolsky) Bar  
Design, Testing and Applications

Chen, W.W.; Song, B.

2011, IX, 388 p., Hardcover

ISBN: 978-1-4419-7981-0